International Journal of Heat and Mass Transfer 52 (2009) 4413–4425

Contents lists available at ScienceDirect

International Journal of Heat and Mass Transfer

journal homepage: www.elsevier.com/locate/ijhmt

# Natural convection flow simulation for various angles in a trapezoidal enclosure with linearly heated side wall(s)

Tanmay Basak [a], S. Roy [b], Amit Singh [b], Bishun D. Pandey [c,*]

[a] Department of Chemical Engineering, Indian Institute of Technology Madras, Chennai 600036, India
[b] Department of Mathematics, Indian Institute of Technology Madras, Chennai 600036, India
[c] Department of Mathematics, The Ohio State University, Marion, OH 43302, USA

ARTICLE INFO

*Article history:*
Received 9 April 2008
Received in revised form 18 March 2009
Accepted 18 March 2009
Available online 6 June 2009

*Keywords:*
Penalty finite element method
Natural convection
Trapezoidal cavity
Linearly heating

ABSTRACT

Natural convection in trapezoidal enclosures for uniformly heated bottom wall, linearly heated vertical wall(s) in presence of insulated top wall have been investigated numerically with penalty finite element method. Parametric studies for the wide range of Rayleigh numbers ($Ra = 10^3 - 10^5$) and Prandtl numbers ($Pr = 0.7 - 1000$) with various tilt angles of side walls ($\varphi$) have been performed. For linearly heated side walls, symmetry in flow pattern is observed. In addition, secondary circulations are observed near the bottom wall for $\varphi = 0^\circ$ especially for larger $Pr$($Pr \geqslant 0.7$). In contrast, for linearly heated left wall and cooled right wall, the secondary circulations are stronger near the top portion of the left wall especially for larger $Pr$. Streamlines show that the strength of convection is larger for $\varphi = 45^\circ$ and flow intensities are found to be larger for higher Prandtl numbers. Local heat transfer rates are found to be relatively larger for $\varphi = 0^\circ$. Average Nusselt number plots show higher heat transfer rates for $\varphi = 0^\circ$ and the overall heat transfer rates at the bottom wall is larger for the linearly heated left wall and cooled right wall. A non-monotonic trend in average Nusselt number vs Rayleigh number due to presence of multiple circulations is observed for $\varphi = 0^\circ$.



## 1. Introduction

Natural convection due to thermal buoyancy effects occurs in various applications of science and technology. Natural convection flows are particularly complex involving several parameters among which the geometry concerned and thermophysical characteristics of the fluid are the most important. The proper dimensions of systems in various applications are supported by experimental studies or/and numerical simulation. Convective heating processes are widely used in food industries [1–6]. Various applications depend on the product specification, shape of the container and heating characteristics. Numerical modeling can offer a way to reduce expensive experimental costs.

A significant amount of earlier studies involve various applications in thermal processing within materials. Rabiey et al. [1] studied transient temperature and fluid flow during natural convection which involves heating of a cylindrical can containing large food particles. Ghani et al. [2] have investigated natural convection within a can of liquid food during sterilization. Various other studies involving sterilization and solidification of foods were reported by earlier researchers [3–5]. Fargue et al. [6] studied separation of natural oils from food substances for industrial applications. A significant number of applications on thermal processing further requires a comprehensive understanding of heat transfer and flow circulations within cavities.

Conduction, natural convection and forced convection are important means of heat transfer in food applications. A comprehensive review by Bejan [7] highlights that internal natural convection flow problems are more complex than external ones. A few studies on steady natural convection within cavities have been carried out by earlier researchers, Gebhart [8] and Hoogendoorn [9] emphasized various aspects of natural convection flows in a square cavity. There are extensive studies available in literature for various square or rectangular cavities [10–17].

A few investigations on natural convection within trapezoidal enclosures have been carried out by earlier researchers [18–34]. Iyican and Bayazitoglu [18–34] investigated the natural convective flow and heat transfer within a trapezoidal enclosure with parallel cylindrical top and bottom walls at different temperatures and plane adiabatic side walls. Karyakin [19] reported two dimensional laminar natural convection in isosceles trapezoidal cavity. The heat transfer rate is found to increase with the increase in base angle. Peric [20] studied natural convection in a trapezoidal cavities using control volume method and observed the convergence of results for grid independent solutions. Kuyper and Hoogendoorn [21] investigated laminar natural convection flow in trapezoidal enclosures to study the influence of the inclination angle on the flow and

* Corresponding author.
*E-mail address:* pandey.1@osu.edu (B.D. Pandey).

0017-9310/$ - see front matter © 2009 Elsevier Ltd. All rights reserved.
doi:10.1016/j.ijheatmasstransfer.2009.03.057

**Nomenclature**

| | |
|---|---|
| $g$ | acceleration due to gravity, $ms^{-2}$ |
| $k$ | thermal conductivity, $Wm^{-1}K^{-1}$ |
| $H$ | height of the trapezoidal cavity |
| $Nu$ | local Nusselt number |
| $\overline{Nu}$ | average Nusselt number |
| $p$ | pressure, |
| $P$ | dimensionless pressure |
| $Pr$ | Prandtl number |
| $Ra$ | Rayleigh number |
| $T$ | temperature, K |
| $T_h$ | temperature of hot bottom wall, K |
| $T_c$ | temperature of cold vertical wall, K |
| $u$ | $x$ component of velocity |
| $U$ | $x$ component of dimensionless velocity |
| $v$ | $y$ component of velocity |
| $V$ | $y$ component of dimensionless velocity |
| $X$ | dimensionless distance along $x$ coordinate |
| $Y$ | dimensionless distance along $y$ coordinate |

*Greek symbols*

| | |
|---|---|
| $\alpha$ | thermal diffusivity, $m^2s^{-1}$ |
| $\beta$ | volume expansion coefficient, $K^{-1}$ |
| $\gamma$ | Penalty parameter |
| $\theta$ | dimensionless temperature |
| $\nu$ | kinematic viscosity, $m^2s^{-1}$ |
| $\varphi$ | angle of inclination of the left wall |
| $\rho$ | density, $kgm^{-3}$ |
| $\Phi$ | basis functions |
| $\psi$ | stream function |
| $\xi$ | horizontal coordinate in a trapezoidal |
| $\eta$ | vertical coordinate in a trapezoidal |

*Subscripts*

| | |
|---|---|
| $b$ | bottom wall |
| $s$ | side wall |

also the dependence of the average Nusselt number on the Rayleigh number. Sadat and Salagnac [22] carried out numerical investigations on solution of laminar natural convection using vorticity–stream function formulation. Steady state solutions were obtained for aspect ratios 3 and 6 and finally, they presented flow patterns and average heat transfer characteristics.

A number of studies on natural convection within trapezoidal enclosures involve various applications. A preliminary investigation on double diffusive convection in trapezoidal enclosures is carried out by Dong and Ebadian [23]. Nguyen et al. [24] studied double diffusive convection within porous trapezoidal enclosure with oblique principal axes. Eyden et al. [25] presented numerical and experimental results for turbulent double diffusive convection of a mixture of two gases in a trapezoidal enclosure with imposed unstable thermal stratification. The numerical results on mean velocity, temperature and concentration, show satisfactory agreement with measurements, indicating that despite some deficiencies, the numerical model can reproduce most of the essential features of the process. Further, Papanicolaou and Belessiotis [26] studied numerically double-diffusive natural convection in asymmetric trapezoidal enclosure. Their numerical investigation is based on a two-equation, low-Reynolds number turbulence model involving a curvilinear coordinate system. Their numerical solutions yield a multi-cellular flow field, with the number of cells depending on the Rayleigh number for a fixed Lewis number and geometry. Later, they analyzed double diffusive natural convection for asymmetric and equivalent rectangular enclosures [27]. Moukalled and coworkers [28–33] studied natural convection within trapezoidal enclosures for applications involving partitioned cavity or baffles on walls within cavity. Recently, Varol et al. [34] studied numerically natural convection within various inclined porous trapezoidal enclosures. Although a few studies of convective heating patterns within trapezoidal containers appear in literature, various applications in food processing involving uniform and non-uniform heating have not yet been analyzed. Thus, comprehensive analysis on natural convection flow within a trapezoidal enclosure is important.

The present study deals with the natural convection within trapezoidal enclosures where the bottom wall is uniformly heated, vertical wall(s) are linearly heated or cooled whereas the top wall is well insulated. This situation may be applied in industrial processing and linear heating may typically occur with a heat source at the bottom. The effect of geometry has been illustrated for various angle of the sidewall varying within 0°—45°. The consistent penalty finite element method [35–38] has been used to solve the nonlinear coupled partial differential equations for flow and temperature fields. Numerical results are presented in terms of isotherm and stream function contours along with the local and average heat transfer rates (Nusselt numbers).

## 2. Mathematical formulation

Let us consider a trapezoidal cavity with the left wall inclined at an angle $\varphi$ with the $y$ axis as seen in Fig. 1(a). The velocity boundary conditions are considered as no-slip on solid boundaries. The liquid material is considered as incompressible, Newtonian and the flow is assumed to be laminar. For the treatment of the buoyancy term in the momentum equation, Boussinesq approximation is employed for the equation of the vertical component of velocity to account for the variations of density as a function of temperature, and to couple in this way the temperature field to the flow field. The governing equations for steady natural convection flow using conservation of mass, momentum and energy in dimensionless form can be written as:

$$\frac{\partial U}{\partial X}+\frac{\partial V}{\partial Y}=0, \tag{1}$$

$$U\frac{\partial U}{\partial X}+V\frac{\partial U}{\partial Y}=-\frac{\partial P}{\partial X}+Pr\left(\frac{\partial^2 U}{\partial X^2}+\frac{\partial^2 U}{\partial Y^2}\right), \tag{2}$$

$$U\frac{\partial V}{\partial X}+V\frac{\partial V}{\partial Y}=-\frac{\partial P}{\partial Y}+Pr\left(\frac{\partial^2 V}{\partial X^2}+\frac{\partial^2 V}{\partial Y^2}\right)+Ra\ Pr\ \theta, \tag{3}$$

$$U\frac{\partial \theta}{\partial X}+V\frac{\partial \theta}{\partial Y}=\frac{\partial^2 \theta}{\partial X^2}+\frac{\partial^2 \theta}{\partial Y^2}. \tag{4}$$

where

$$X=\frac{x}{H},\quad Y=\frac{y}{H},\quad U=\frac{uH}{\alpha},\quad V=\frac{vH}{\alpha},$$

$$P=\frac{pH^2}{\rho\alpha^2},\quad \theta=\frac{T-T_c}{T_h-T_c},\quad Pr=\frac{\nu}{\alpha},\quad Ra=\frac{g\beta(T_h-T_c)L^3}{\nu\alpha}, \tag{5}$$

with following boundary conditions

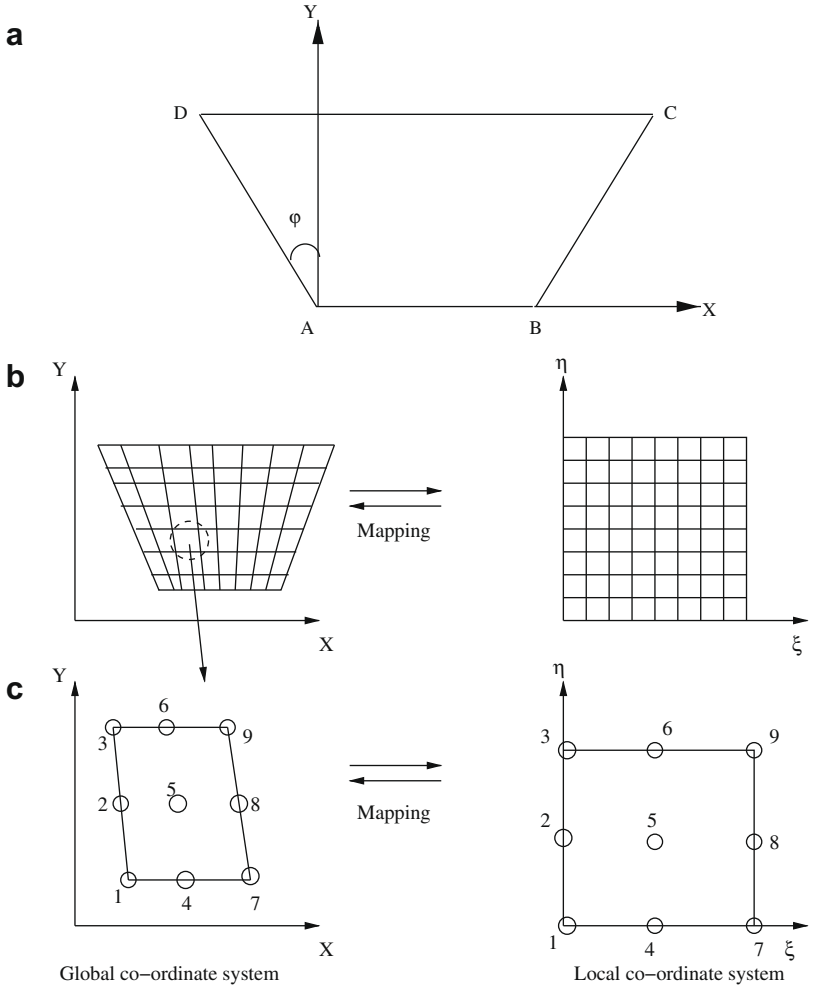


**Fig. 1.** (a) Schematic diagram of the physical system where $\varphi(0^\circ,\ 30^\circ$ or $45^\circ)$ denotes the angle of inclination with $Y$ axis, (b) the mapping of trapezoidal domain in $x-y$ coordinate system to a square domain in $\xi-\eta$ coordinate system and (c) the mapping of an individual element to a single element in $\xi-\eta$ coordinate system.

$$
\begin{aligned}
&U=0,\ \ V=0,\ \ \theta=1,\ \ \forall Y=0,\ \ 0\leqslant X\leqslant 1,\\
&U=0,\ \ V=0,\ \ \theta=1-Y,\ \ \forall X\cos(\varphi)+Y\sin(\varphi)=0,\ \ 0\leqslant Y\leqslant 1,\\
&U=0,\ \ V=0,\ \ \theta=1-Y \text{ or } 0,\ \ \forall X\cos(\varphi)-Y\sin(\varphi)=\cos(\varphi),\ \ 0\leqslant Y\leqslant 1,\\
&U=0,\ \ V=0,\ \ \tfrac{\partial\theta}{\partial Y}=0,\ \ \forall Y=1,\ \ -\tan(\varphi)\leqslant X\leqslant 1+\tan(\varphi).
\end{aligned}
\tag{6}
$$

## 3. Solution procedure

The momentum and energy balance equations Eqs. (2)–(4) are solved using Galerkin finite element method. The continuity equation (Eq. (1)) is used as a constraint due to mass conservation and this constraint may be used to obtain the pressure distribution [35–37]. In order to solve Eqs. (2) and (3), the penalty finite element method has been used where the pressure $P$ is eliminated by a penalty parameter $\gamma$ and the incompressibility criteria given by Eq. (1) as (see Reddy [35])

$$P=-\gamma\left(\frac{\partial U}{\partial X}+\frac{\partial V}{\partial Y}\right). \tag{7}$$

The continuity equation (Eq. (1)) is automatically satisfied for large values of $\gamma$. Typical value of $\gamma$ that yield consistent solutions is $10^7$ [35–37].

Using Eq. (7), the momentum balance equations (Eqs. (2) and (3)) reduce to

$$U\frac{\partial U}{\partial X}+V\frac{\partial U}{\partial Y}=\gamma\frac{\partial}{\partial X}\left(\frac{\partial U}{\partial X}+\frac{\partial V}{\partial Y}\right)+Pr\left(\frac{\partial^2 U}{\partial X^2}+\frac{\partial^2 U}{\partial Y^2}\right), \tag{8}$$

and

$$U\frac{\partial V}{\partial X}+V\frac{\partial V}{\partial Y}=\gamma\frac{\partial}{\partial Y}\left(\frac{\partial U}{\partial X}+\frac{\partial V}{\partial Y}\right)+Pr\left(\frac{\partial^2 V}{\partial X^2}+\frac{\partial^2 V}{\partial Y^2}\right)+Ra\ Pr\ \theta. \tag{9}$$

Expanding the velocity components $(U,V)$ and temperature $(\theta)$ using basis set $\{\Phi_k\}_{k=1}^N$ as,

$$
\begin{aligned}
&U\approx\sum_{k=1}^{N}U_k\Phi_k(X,Y),\quad V\approx\sum_{k=1}^{N}V_k\Phi_k(X,Y),\quad \text{and}\\
&\theta\approx\sum_{k=1}^{N}\theta_k\Phi_k(X,Y),
\end{aligned}
\tag{10}
$$

the Galerkin finite element method yields the following nonlinear residual equations for Eqs. (8), (9) and (4), respectively, at nodes of internal domain $\Omega$:

$$R_i^{(1)} = \sum_{k=1}^{N} U_k \int_\Omega \left[ \left( \sum_{k=1}^{N} U_k \Phi_k \right) \frac{\partial \Phi_k}{\partial X} + \left( \sum_{k=1}^{N} V_k \Phi_k \right) \frac{\partial \Phi_k}{\partial Y} \right] \Phi_i \, dX \, dY + \gamma \left[ \sum_{k=1}^{N} U_k \int_\Omega \frac{\partial \Phi_i}{\partial X} \frac{\partial \Phi_k}{\partial X} dX \, dY + \sum_{k=1}^{N} V_k \int_\Omega \frac{\partial \Phi_i}{\partial X} \frac{\partial \Phi_k}{\partial Y} dX \, dY \right] + Pr \sum_{k=1}^{N} U_k \int_\Omega \left[ \frac{\partial \Phi_i}{\partial X} \frac{\partial \Phi_k}{\partial X} + \frac{\partial \Phi_i}{\partial Y} \frac{\partial \Phi_k}{\partial Y} \right] dX \, dY \quad (11)$$

$$R_i^{(2)} = \sum_{k=1}^{N} V_k \int_\Omega \left[ \left( \sum_{k=1}^{N} U_k \Phi_k \right) \frac{\partial \Phi_k}{\partial X} + \left( \sum_{k=1}^{N} V_k \Phi_k \right) \frac{\partial \Phi_k}{\partial Y} \right] \Phi_i \, dX \, dY + \gamma \left[ \sum_{k=1}^{N} U_k \int_\Omega \frac{\partial \Phi_i}{\partial Y} \frac{\partial \Phi_k}{\partial X} dX \, dY + \sum_{k=1}^{N} V_k \int_\Omega \frac{\partial \Phi_i}{\partial Y} \frac{\partial \Phi_k}{\partial Y} dX \, dY \right] + Pr \sum_{k=1}^{N} V_k \int_\Omega \left[ \frac{\partial \Phi_i}{\partial X} \frac{\partial \Phi_k}{\partial X} + \frac{\partial \Phi_i}{\partial Y} \frac{\partial \Phi_k}{\partial Y} \right] dX \, dY - Ra \, Pr \times \int_\Omega \left( \sum_{k=1}^{N} \theta_k \Phi_k \right) \Phi_i \, dX \, dY \quad (12)$$

and

$$R_i^{(3)} = \sum_{k=1}^{N} \theta_k \int_\Omega \left[ \left( \sum_{k=1}^{N} U_k \Phi_k \right) \frac{\partial \Phi_k}{\partial X} + \left( \sum_{k=1}^{N} V_k \Phi_k \right) \frac{\partial \Phi_k}{\partial Y} \right] \Phi_i \, dX \, dY + \sum_{k=1}^{N} \theta_k \int_\Omega \left[ \frac{\partial \Phi_i}{\partial X} \frac{\partial \Phi_k}{\partial X} + \frac{\partial \Phi_i}{\partial Y} \frac{\partial \Phi_k}{\partial Y} \right] dX \, dY. \quad (13)$$

The set of non-linear algebraic equations (Eqs. (11)–(13)) are solved using reduced integration technique [39] and Newton Raphson method as discussed in earlier work [36,37].

## 4. Evaluation of stream function and Nusselt number

### 4.1. Stream function

The fluid motion is displayed using the stream function $\psi$ obtained from velocity components $U$ and $V$. The relationships between stream function, $\psi$ (see Batchelor [40]) and velocity components for two dimensional flows are

$$U = \frac{\partial \psi}{\partial Y}, \quad V = -\frac{\partial \psi}{\partial X}, \quad (14)$$

which yield a single equation

$$\frac{\partial^2 \psi}{\partial X^2} + \frac{\partial^2 \psi}{\partial Y^2} = \frac{\partial U}{\partial Y} - \frac{\partial V}{\partial X}. \quad (15)$$

It may be noted that the positive sign of $\psi$ denotes anti-clockwise circulation and the clockwise circulation is represented by the negative sign of $\psi$. The no-slip condition is valid at all boundaries as there is no cross flow, hence $\psi = 0$ is used for the boundaries. Expanding the stream function $(\psi)$ using the basis set $\{\Phi\}$ as $\psi = \sum_{k=1}^{N} \psi_k \Phi_k(X, Y)$ and the relation for $U$, $V$, the Galerkin finite element method yields the following linear residual equations for Eq. (15).

$$R_i^s = \sum_{k=1}^{N} \psi_k \int_\Omega \left[ \frac{\partial \Phi_i}{\partial X} \frac{\partial \Phi_k}{\partial X} + \frac{\partial \Phi_i}{\partial Y} \frac{\partial \Phi_k}{\partial Y} \right] dX \, dY + \sum_{k=1}^{N} U_k \int_\Omega \Phi_i \frac{\partial \Phi_k}{\partial Y} dX \, dY - \sum_{k=1}^{N} V_k \int_\Omega \Phi_i \frac{\partial \Phi_k}{\partial X} dX \, dY \quad (16)$$

The no-slip condition is valid at all boundaries as there is no cross flow, hence $\psi = 0$ is used as residual equations at the nodes for the boundaries. The bi-quadratic basis function is used to evaluate the integrals in Eq. (16) and $\psi$'s are obtained by solving the $N$ linear residual equations.

### 4.2. Nusselt number

The heat transfer coefficient in terms of the local Nusselt number $(Nu)$ is defined by

$$Nu = -\frac{\partial \theta}{\partial n}, \quad (17)$$

where $n$ denotes the normal direction on a plane. The normal derivative is evaluated by the bi-quadratics basis set in $\xi - \eta$ domain. The local Nusselt numbers at bottom wall $(Nu_b)$, left wall $(Nu_l)$ and right wall $(Nu_r)$ are defined as

$$Nu_b = \sum_{i=1}^{9} \theta_i \frac{\partial \Phi_i}{\partial Y}, \quad (18)$$

$$Nu_l = \sum_{i=1}^{9} \theta_i \left( cos\varphi \frac{\partial \Phi_i}{\partial X} + sin\varphi \frac{\partial \Phi_i}{\partial Y} \right). \quad (19)$$

and

$$Nu_r = \sum_{i=1}^{9} \theta_i \left( -cos\varphi \frac{\partial \Phi_i}{\partial X} + sin\varphi \frac{\partial \Phi_i}{\partial Y} \right). \quad (20)$$

The average Nusselt numbers at the bottom, left and right walls are

$$\overline{Nu_b} = \frac{\int_0^1 Nu_b dX}{X|_0^1} = \int_0^1 Nu_b dX, \quad (21)$$

$$\overline{Nu_l} = cos\varphi \int_0^{\frac{1}{cos\varphi}} Nu_l ds_1, \quad (22)$$

and

$$\overline{Nu_r} = cos\varphi \int_0^{\frac{1}{cos\varphi}} Nu_r ds_2, \quad (23)$$

where $ds_1$ and $ds_2$ are the small elemental lengths along the left and right walls, respectively.

## 5. Results and discussion

### 5.1. Numerical tests

Numerical simulations are performed for $Pr = 0.7$ (air), $Pr = 10$ (fruit juice) and $Pr = 1000$ (olive oil) with $10^3 \leqslant Ra \leqslant 10^5$ for various inclination angle ($\varphi = 45^\circ, 30^\circ$ and $0^\circ$) (see Fig. 1a). The computational domain consists of $20 \times 20$ bi-quadratic elements which correspond to $41 \times 41$ grid points in $\xi - \eta$ domain as discussed in Appendix A; Fig. 1b and c. The fluid motion and heating patterns are studied for uniformly heated bottom wall with either linearly heated side walls or linear heated left wall with cooled right wall in presence of adiabatic top wall.

It may be noted that, the jump discontinuity in Dirichlet type of wall boundary conditions at the right corner point in case of hot bottom wall and right cold wall corresponds to computational singularity. In particular, the singularity at the right corner of the bottom wall needs special attention. To ensure the convergence of the numerical solution to the exact solution, the grid sizes have been optimized and computed results are found to be independent of grid sizes. The grid size dependent effect upon the Nusselt numbers (local and average) due to temperature discontinuity at the corner point tends to increase as the mesh spacing at the corner is reduced. One of the ways for handling the problem is assuming the average temperature of the two walls at the corner and keeping the adjacent grid-nodes at the respective wall temperatures. Alternatively, based on earlier work by Ganzarolli and Milanez [41], once any corner formed by the intersection of two differentially heated boundary walls is assumed at the average temperature of the adjacent walls, the optimal grid size obtained for each

configuration corresponds to the mesh spacing over which further grid refinements lead to grid invariant results in both heat transfer rates and flow fields.

In the current investigation, Gaussian quadrature based finite element method provides the smooth solutions at the interior domain including the corner regions as evaluation of residual depends on interior Gauss points and thus the effect of corner nodes is less pronounced in the final solution. In general, the Nusselt numbers for finite difference/finite volume based methods are calculated at any surface using some interpolation functions [20,21,42] which are now avoided in the current work. The present finite element approach offers special advantage on evaluation of local Nusselt number at the bottom and side walls as the element basis functions are used to evaluate the heat flux. Flow and temperature fields are shown in terms of streamlines and isotherms, respectively.

Isotherms and streamlines for a square cavity ($\varphi = 0^\circ$) with hot left wall and cold right wall in presence of adiabatic horizontal walls have been benchmarked with an earlier work [42]. It may be noted that current simulation studies are based on $20 \times 20$ biquadratic elements or $41 \times 41$ grid and further refinement of grids did not produce any significant change on temperature, streamfunctions and Nusselt numbers for $Ra \leqslant 10^5$. The results based on current simulation strategy are shown in Fig. 2 and simulation results are in good agreement with the earlier result [42]. Overall heat transfer rates are estimated based on average Nusselt numbers. It is found that $\overline{Nu}$ is within 2.25–2.3 for $Ra = 10^4$ and 4.55–4.6 for $Ra = 10^5$ based on current work and the earlier study [42].

### 5.2. Linearly heated side walls

Figs. 3–7 illustrate isotherms and streamlines for $Ra = 10^3 - 10^5$ with $Pr = 0.7 - 1000$ in presence of uniformly heated bottom wall and linearly heated side walls. As expected due to linearly heated vertical walls and uniformly heated bottom wall, fluids rise up from the middle portion of the bottom wall and flow down along the two vertical walls forming two symmetric rolls with clockwise and anticlockwise rotations inside the cavity. For $Ra = 10^3$, the magnitudes of stream function are considerably smaller and the heat transfer is purely due to conduction as seen in Fig. 3a–c. The temperature contours with $\theta = 0.1 - 0.7$ occur symmetrically near the side walls of the enclosure for $Ra = 10^3$ with $\varphi = 45^\circ$ (Fig. 3a). The other temperature contours with $\theta \geqslant 0.8$ are smooth curves symmetric with respect to vertical symmetric line at the center. The isotherms with $\theta = 0.1 - 0.6$ occur symmetrically near the side walls of the enclosure with $\varphi = 30^\circ$ (Fig. 3b) whereas $\theta \geqslant 0.7$ are smooth curves symmetric with respect to vertical symmetric line. For square cavity ($\varphi = 0^\circ$), the isotherms with $\theta = 0.1 - 0.3$ are symmetric along the side walls and $\theta \geqslant 0.4$ are smooth curves symmetric with respect to the vertical symmetric line (Fig. 3c). It is interesting to observe that more isotherms with larger magnitudes are pushed towards the side walls for larger $\varphi$'s. This is due to fact that the intensity of circulation is maximum for $\varphi = 45^\circ$ whereas the less circulation is observed for $\varphi = 0^\circ$. Note that, the maximum value of stream function ($|\psi|_{max}$) is 0.24 for $\varphi = 45^\circ$ (Fig. 3a) and $|\psi|_{max}$ for $\varphi = 0^\circ$ (Fig. 3c).

During conduction dominant heat transfer, the temperature profiles are almost invariant with respect to $Ra$ for specific $\varphi$ and it is observed that the significant convection is initiated at $Ra = 5 \times 10^3$ for $\varphi = 45^\circ$ and $30^\circ$, and at $Ra = 10^4$ for $\varphi = 0^\circ$ (Fig. 4). At critical $Ra$, the distortion of the isotherm gradually increases and convection becomes dominant mode of heat transfer. At the onset of convection, continuous isotherm contours break into two discrete contours and move towards the sidewalls. The isotherms with $\theta = 0.8, 0.7$ and 0.5 break into two symmetric contours near the side wall of the enclosure for $\varphi = 45^\circ$, $30^\circ$ and $0^\circ$, respectively. It is also interesting to observe that the discrete isotherms near the side walls get compressed near the walls due to enhanced circulations. It may be noted that $|\psi|_{max}$ are 1.6, 1.5 and 1.4, for $\varphi = 45^\circ$, $30^\circ$ and $0^\circ$, respectively Fig. 4(a)–(c).

As $Ra$ increases to $10^5$, the effect of buoyancy force is stronger compared to viscous force and greater circulations near the central core of each half of the enclosure are observed. Small thermal gradient occurs at the central regime whereas a large stratification zone of temperature is observed at the vertical symmetric line near the bottom wall due to stagnation of flow Fig. 5(a)–(c). It is also observed that isotherms are compressed strongly towards the side

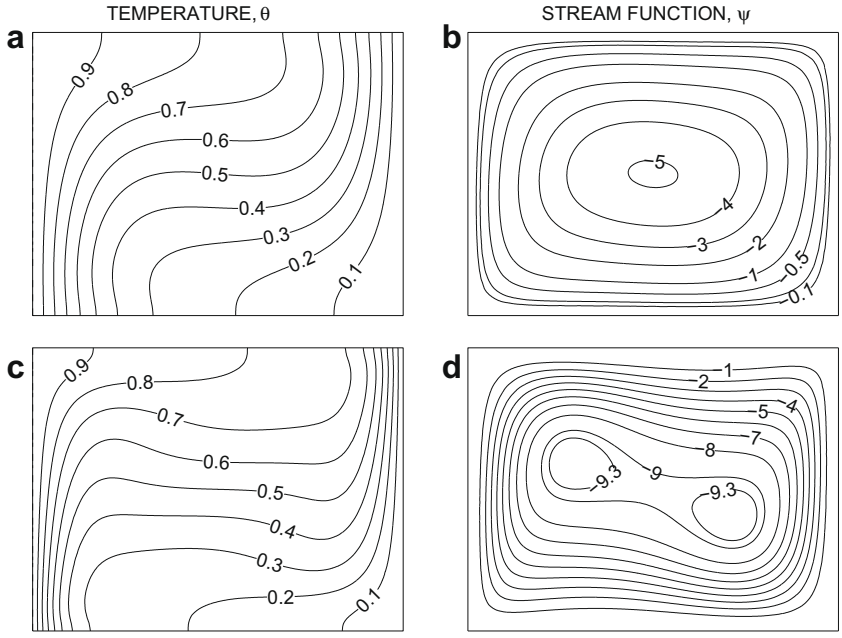


**Fig. 2.** Isotherms and streamlines for a benchmark problem [42] involving natural convection of a model fluid ($Pr = 0.71$) within a square cavity ($\varphi = 0^\circ$) for hot left wall and cold right wall in presence of adiabatic horizontal walls for $Ra = 10^4$ (a and b) and $Ra = 10^5$ (c and d).

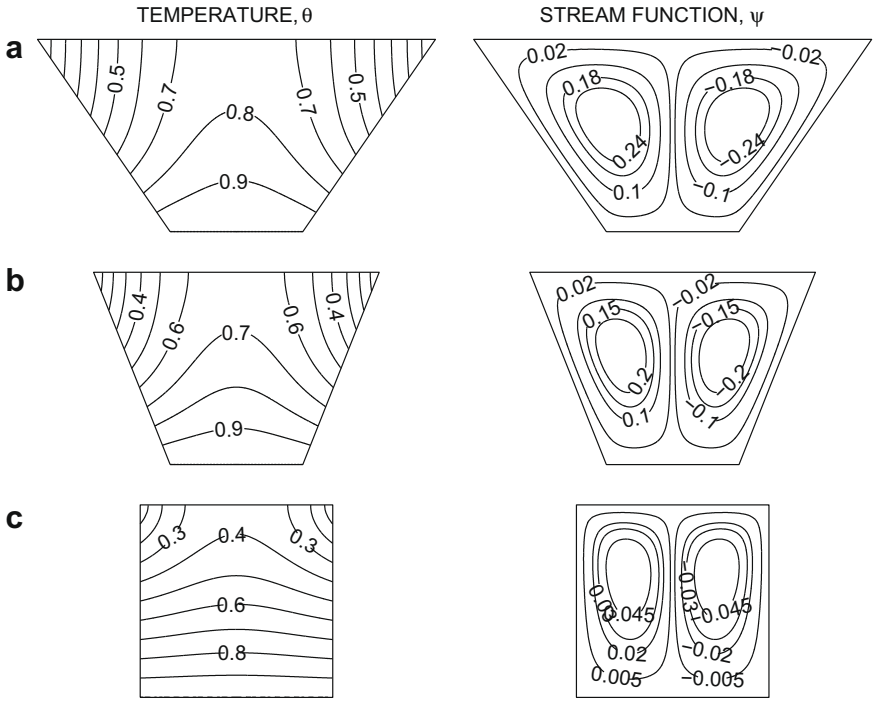


**Fig. 3.** Isotherms and streamlines for linearly heated side walls with $Pr = 0.7$ and $Ra = 10^3$ for (a) $\varphi = 45^\circ$ (b) $\varphi = 30^\circ$ and (c) $\varphi = 0^\circ$. Clockwise and anti-clockwise flows are shown via negative and positive signs of stream functions, respectively.

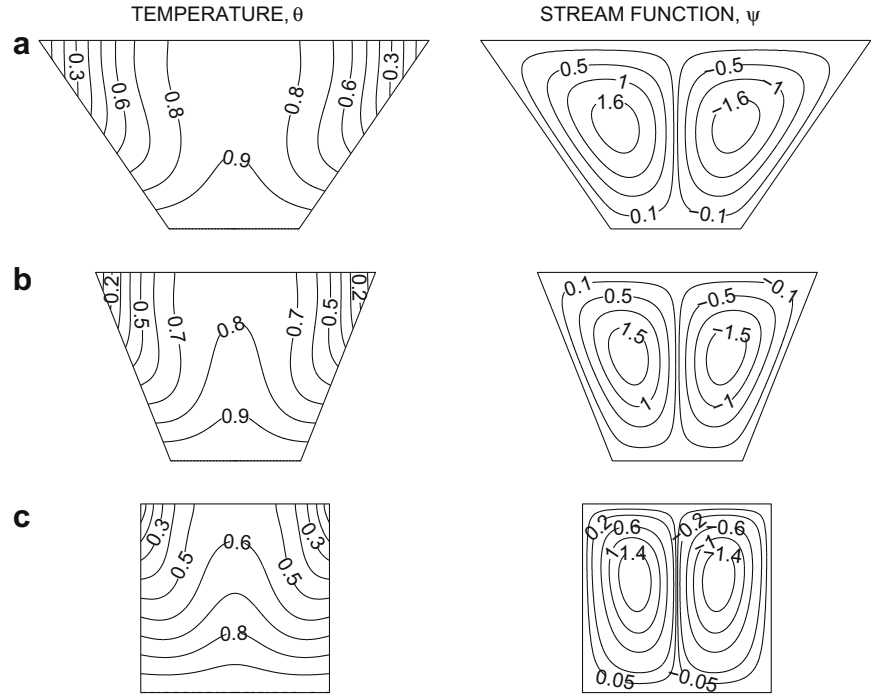


**Fig. 4.** Isotherms and streamlines for linearly heated side walls with $Pr = 0.7$ for (a) $\varphi = 45^\circ$, $Ra = 5 \times 10^3$ (b) $\varphi = 30^\circ$, $Ra = 5 \times 10^3$ (c) $\varphi = 0^\circ$, $Ra = 10^4$. Clockwise and anti-clockwise flows are shown via negative and positive signs of stream functions, respectively.

walls. For example, the isotherms with $\theta \leqslant 0.7$, $\theta \leqslant 0.7$ and $\theta \leqslant 0.5$ are highly compressed near the side walls of the enclosure for $\varphi = 45^\circ$, $30^\circ$ and $0^\circ$, respectively. Isotherms for $\varphi = 45^\circ$ are more distorted (Fig. 5a) compared to $30^\circ$ (Fig. 5b) and $0^\circ$ (Fig. 5c). The shape of streamlines is found to be almost circular except near the side wall. It is interesting to observe that, for $\varphi = 0^\circ$, symmetric secondary circulation with $|\psi|_{max} = 3$ occur near the bottom corners (Fig. 5c). It may be remarked that these secondary circulations are the representatives for low Prandtl number fluid ($Pr = 0.7$). The number of secondary circulations is found to be also dependent on tilt angle and therefore, the tilt angle plays a significant role on thermal mixing within the fluid. In fact, with similar parameter values, the secondary circulations disappear in the present case (Fig. 5(a)–(c)) for the tilt angle, $\theta \geqslant 15^\circ$.

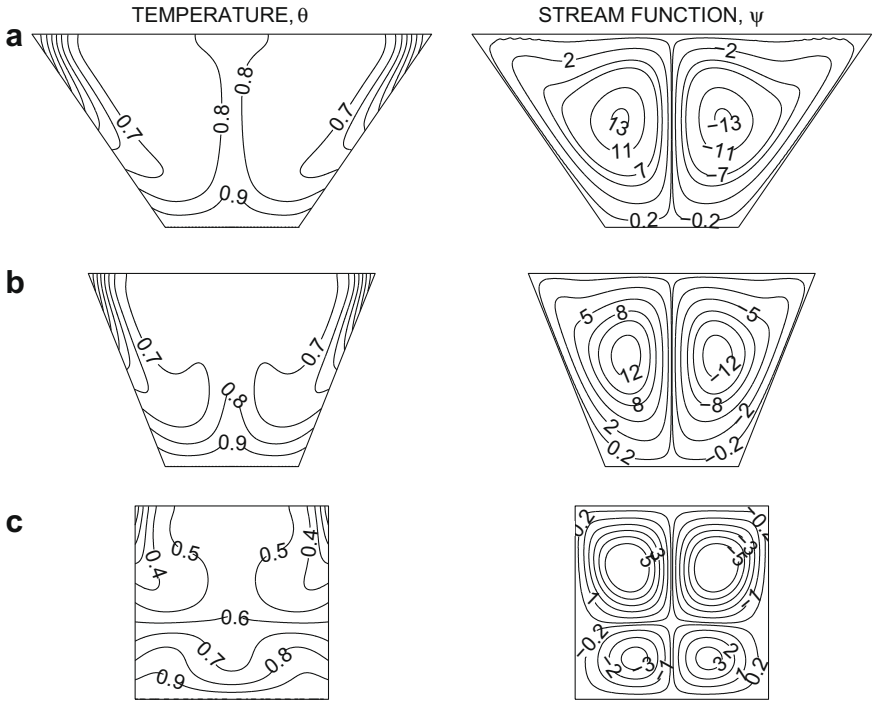


**Fig. 5.** Isotherms and streamlines for linearly heated side walls with $Pr = 0.7$ and $Ra = 10^5$ for (a) $\varphi = 45^\circ$ (b) $\varphi = 30^\circ$ and (c) $\varphi = 0^\circ$. Clockwise and anti-clockwise flows are shown via negative and positive signs of stream functions, respectively.

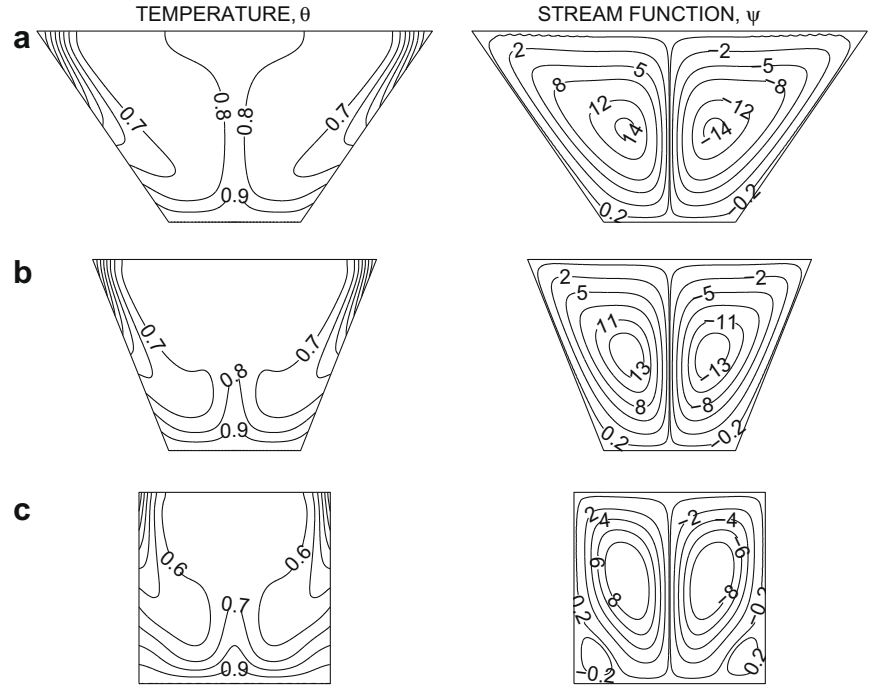


**Fig. 6.** Isotherms and streamlines for linearly heated side walls with $Pr = 10$ and $Ra = 10^5$ for (a) $\varphi = 45^\circ$ (b) $\varphi = 30^\circ$ and (c) $\varphi = 0^\circ$. Clockwise and anti-clockwise flows are shown via negative and positive signs of stream functions, respectively.

At $Ra = 10^5$ for $Pr = 10$ (Fig. 6), the isotherms are strongly compressed towards the top portion of the sidewalls due to higher temperature gradient within the thermal boundary layer. It is observed that the thicknesses of the thermal boundary layers especially at the top portion of side walls are reduced for $Pr = 10$ as compared to $Pr = 0.7$. At higher $Ra$ with $Pr = 10$, the streamlines cover the entire cavity and attain the shape of the container especially for $\varphi = 45^\circ$ and $30^\circ$. For $Pr = 1000$ at $Ra = 10^5$ (Fig. 7), isotherms along the sidewalls get further compressed and thickness of the thermal boundary layer is also reduced. Similar to previous results for lower Prandtl number, streamlines indicate stronger circulations for tilt angle $\varphi = 45^\circ$ and $30^\circ$. The intensity of flow circulations for $Pr = 1000$ is represented with $|\psi|_{max} = 13 - 14$ for $\varphi = 45^\circ$, $|\psi|_{max} = 13 - 14$ for $\varphi = 30^\circ$ and $|\psi|_{max} = 7 - 9$ for $\varphi = 0^\circ$

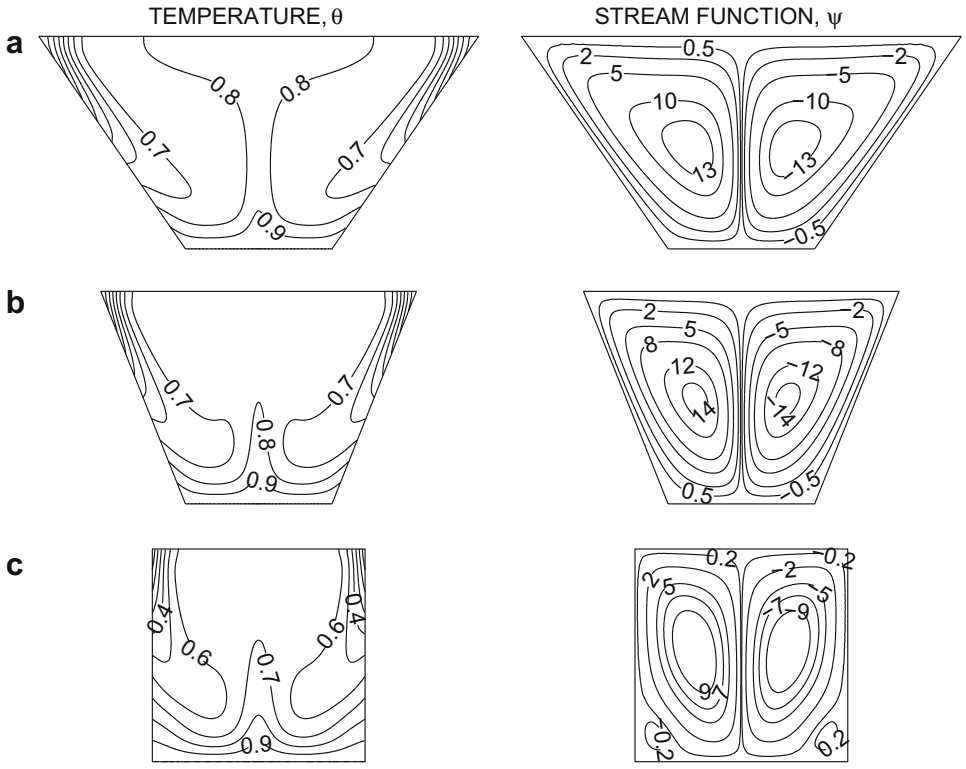


**Fig. 7.** Isotherms and streamlines for linearly heated side walls with $Pr = 1000$ and $Ra = 10^5$ for (a) $\varphi = 45^\circ$ (b) $\varphi = 30^\circ$ and (c) $\varphi = 0^\circ$. Clockwise and anti-clockwise flows are shown via negative and positive signs of stream functions, respectively.

whereas for $Pr = 0.7$, $|\psi|_{max} = 11 - 13$ for $\varphi = 45^\circ, |\psi|_{max} = 12$ for $\varphi = 30^\circ$ and $|\psi|_{max} = 5$ for $\varphi = 0^\circ$ (Figs. 5–7). These values further illustrate higher intensity of convection for higher Prandtl number. It may also be remarked that the larger intensity of circulations for higher $Pr$ fluid causes the shapes of streamlines identical to the outer domain, near to the walls and that signifies enhanced mixing effects. It is interesting to note that for $\varphi = 0^\circ$, higher $Pr$ reduces the strength of the secondary circulation with the enhancement of the strength of primary circulations as higher Prandtl number fluid implies stronger viscous force which makes the secondary circulation weaker.

### 5.3. Linearly heated left wall and with cold right wall

Figs. 8–10 illustrate streamlines and isotherms for $Ra = 10^3 - 10^5$. Due to uniformly heated bottom wall and cold right wall, the singularity appears at the right bottom edge of the cavity. The formation of the thermal boundary layer along the left wall of the cavity is weaker whereas isotherms are compressed along the right wall of the cavity forming strong thermal boundary layer. The symmetric circulation pattern which was observed for linearly heated side walls case is absent in the present case due to non-symmetric thermal boundary conditions. Streamlines closer to the top left wall show secondary circulations whereas streamlines closer to the right wall show stronger primary circulations. Note that, the uniformly heated bottom wall and linearly heated left wall cause the fluids to move with less circulation along the left wall whereas due to the cold right wall, larger amount of fluid flow along the right wall. As a result, strong circulation patterns are formed on the right side of the cavity whereas secondary circulation patterns appear on the left side of the cavity. For $Pr = 0.7$ and $Ra = 10^3$, the magnitude of stream function is considerably smaller and heat transfer is primarily due to conduction as seen in Fig. 8. Temperature contours with $\theta \leqslant 0.6, \theta \leqslant 0.5$ and $\theta \leqslant 0.2$ for $\varphi = 45^\circ$, $30^\circ$ and $0^\circ$, respectively, are compressed to side walls. Similar to uniform heating situation, $|\psi|_{max}$ for primary circulation cell decreases with tilt angle. Note that $|\psi|_{max}$ is 1.1 for $\varphi = 45^\circ$ whereas $|\psi|_{max} = 0.6$ for $\varphi = 0^\circ$. It may also be noted that for $\varphi = 45^\circ$, secondary circulation with $|\psi|_{max} = 0.1$ is found near the top left wall. The value of $\psi_{max}$ for the secondary circulation decreases with the decrease in tilt angle. For $\varphi = 30^\circ$, the maximum value of $\psi$ is 0.08. Further decrease in the tilt angle exhibits no secondary circulation as shown for $\varphi = 0^\circ$ (Fig. 8c).

It is observed that the significant convection is initiated at critical $Ra = 3 \times 10^3$ for $\varphi = 45^\circ$ and $\varphi = 30^\circ$, and at $Ra = 5 \times 10^3$ for $\varphi = 0^\circ$ (Figure not shown). Fig. 9 displays isotherms and streamlines for $Pr = 0.7$ at $Ra = 10^5$. Results indicate that the values of stream functions are larger and isotherms are compressed near the cold wall due to higher intensity of circulations as can be seen in Fig. 9. In particular, for $\varphi = 0^\circ, 30^\circ$ and $45^\circ$, the isotherms with $\theta \leqslant 0.5, \theta \leqslant 0.5$ and $\theta \leqslant 0.4$, respectively, are highly compressed towards the cold wall. It is interesting to observe that the intensity of primary circulation is large irrespective of $\varphi$ and $|\psi|_{max}$ is 18, for $\varphi = 45^\circ, 30^\circ$ and $0^\circ$. It may be noted that secondary circulations become stronger as compared to $Ra = 10^3$ and also, at $Ra = 10^5$, even for tilt angle $\varphi = 0^\circ$, secondary circulation appears with $\psi_{max} = 0.3$. The strength of the secondary circulation increases due to enhanced convection for $\varphi = 30^\circ$ and $45^\circ$. It is found that $\psi_{max}$ of secondary circulations are 4 and 5 for $\varphi = 30^\circ$ and $45^\circ$, respectively. At $Ra = 10^5$, comparative studies on Figs. 9 and 10 for $Pr = 0.7 - 1000$ show that as $Pr$ increases, the values of stream function in the primary circulations also increase and isotherms are highly compressed near cold right wall.

### 5.4. Heat transfer rates: local and average Nusselt numbers

#### 5.4.1. Local Nusselt number: linearly heated side walls

Fig. 11a displays the local heat transfer rate for the bottom wall ($Nu_b$) with $Pr = 0.7$ and $Pr = 10$ and $Ra = 10^3 - 10^5$ for various tilt

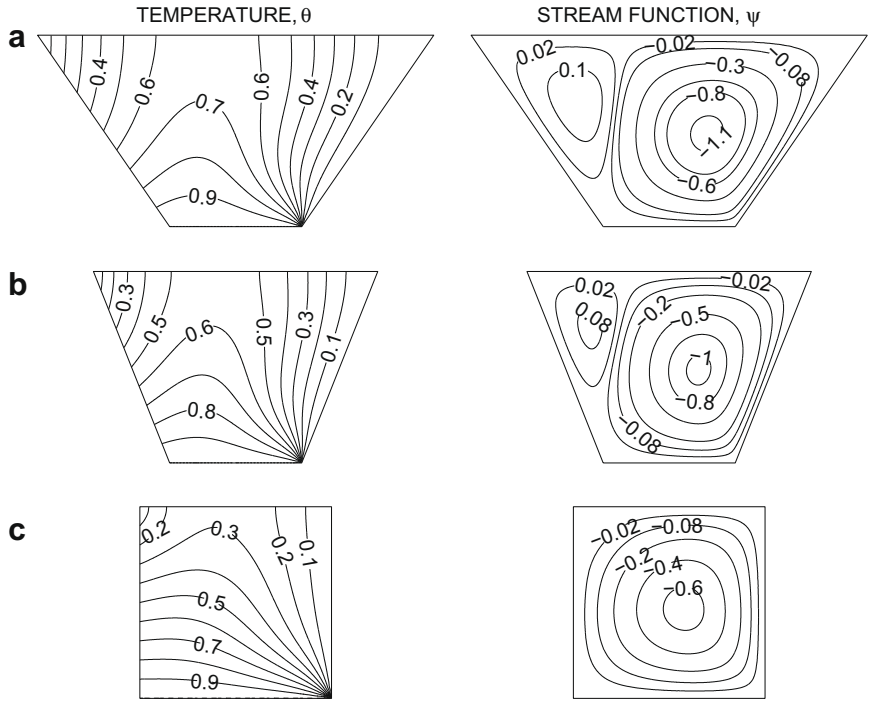


**Fig. 8.** Isotherms and streamlines for linearly heated left vertical wall and cold right vertical wall with $Pr = 0.7$ and $Ra = 10^3$ for (a) $\varphi = 45^\circ$ (b) $\varphi = 30^\circ$ and (c) $\varphi = 0^\circ$. Clockwise and anti-clockwise flows are shown via negative and positive signs of stream functions, respectively.

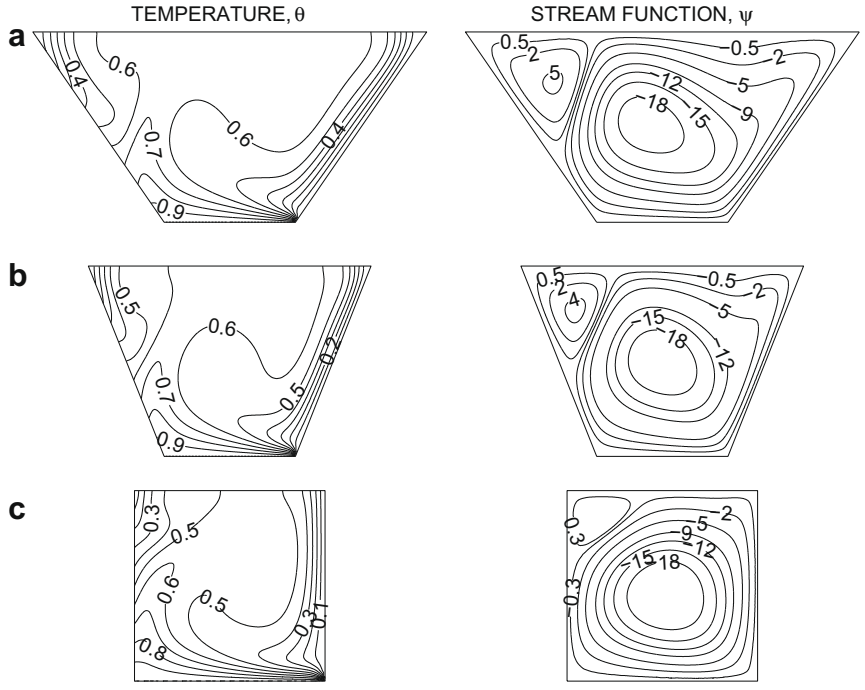


**Fig. 9.** Isotherms and streamlines for linearly heated left vertical wall and cold right vertical wall with $Pr = 0.7$ and $Ra = 10^5$ for (a) $\varphi = 45^\circ$ (b) $\varphi = 30^\circ$ and (c) $\varphi = 0^\circ$. Clockwise and anti-clockwise flows are shown via negative and positive signs of stream functions, respectively.

angles ($\varphi$). Due to the symmetry in the temperature field, heat transfer at the bottom wall is symmetric with respect to the mid length ($X = 1/2$). It is observed that, due to weak circulation, isotherms are widely dispersed along the bottom wall for $Ra = 10^3$ and the local Nusselt number ($Nu_b$) is found to be almost constant throughout the bottom wall as illustrated for $\varphi = 45^\circ$ and $Ra = 10^3$. It is also observed that for $\varphi = 30^\circ$ and $\varphi = 45^\circ$ and $Ra = 10^5$ with both $Pr$ (0.7 and 10), isotherms are widely dispersed at the center of the bottom wall and therefore local Nusselt number has a minimum at $X = 1/2$ except for $\varphi = 0^\circ$ and $Pr = 0.7$. It is interesting to note that, isotherms are compressed around the intermediate zones between corner and vertical line of symmetry, and local Nusselt number is maximum at around $X = 0.3$ and 0.7 at $Ra = 10^5$ except for $\varphi = 0^\circ$. For $\varphi = 0^\circ$ with $Ra = 10^5$ and $Pr = 0.7$,

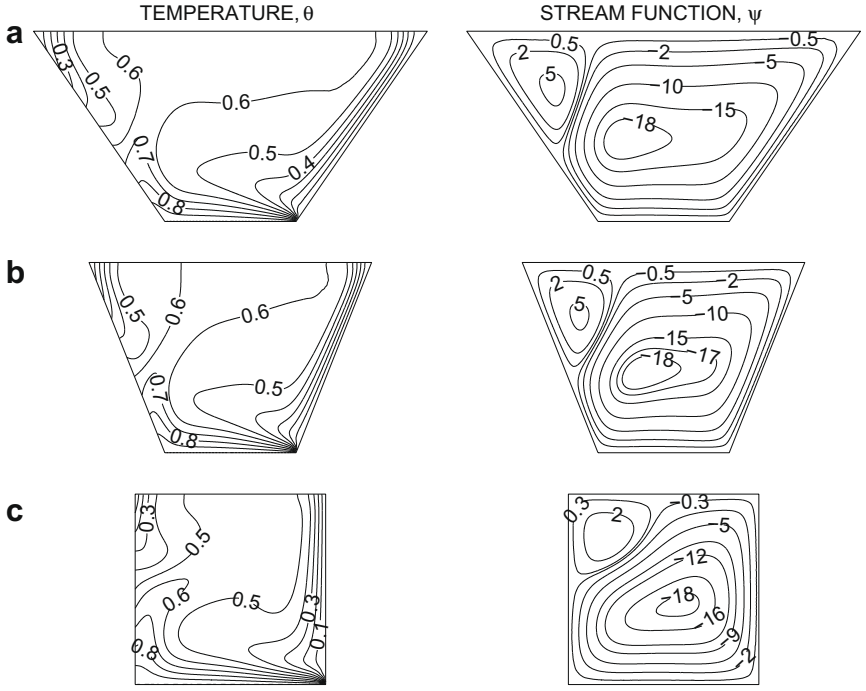


**Fig. 10.** Isotherms and streamlines for linearly heated left vertical wall and cold right vertical wall with $Pr = 1000$ and $Ra = 10^5$ for (a) $\varphi = 45^\circ$ (b) $\varphi = 30^\circ$ and (c) $\varphi = 0^\circ$. Clockwise and anti-clockwise flows are shown via negative and positive signs of stream functions, respectively.

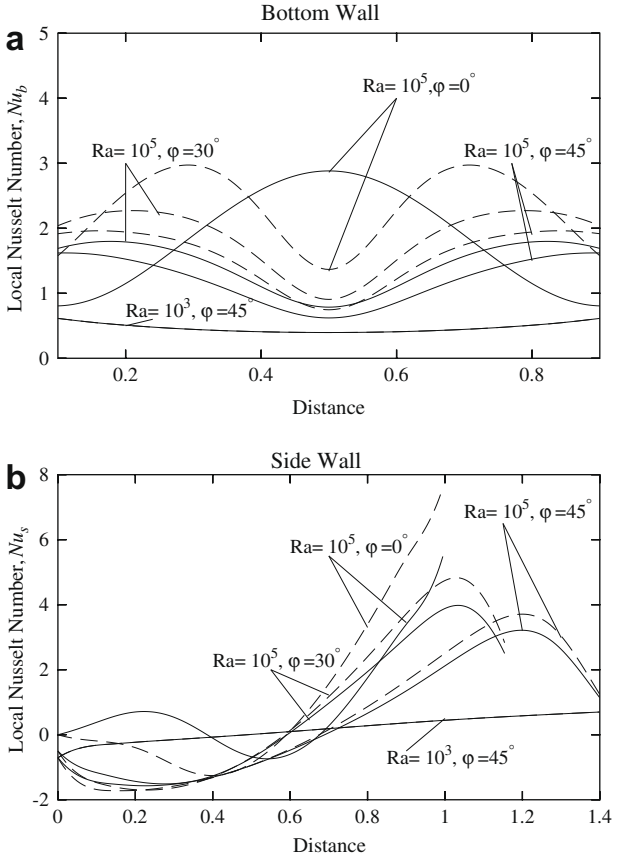


**Fig. 11.** Variation of local Nusselt number with distance along (a) bottom wall (b) side wall for $Pr = 0.7$ (—) and $Pr = 10$ (- - -) with linearly heated side walls.

the heat transfer rate is maximum at the center due to the presence of strong secondary circulations leading to a high temperature gradient at the center of bottom wall. Variations of Prandtl numbers from $Pr = 0.7$ to 10 at $Ra = 10^5$ show only a slight increase in the value of local Nusselt numbers for $\varphi = 45^\circ$ and $30^\circ$. It is interesting to observe that $Nu_b$ distribution follows similar qualitative trends for $\varphi = 0^\circ - 45^\circ$ as the secondary circulation at the central regime of the bottom wall almost disappears at higher $Pr$ ($Pr = 10$, see Fig. 11a).

Heat transfer rates at the side wall for linearly heated side wall for $Pr = 0.7$ and 10 is illustrated in Fig. 11(b). Due to the symmetry in the boundary condition, the local Nusselt number is identical along both the side walls. For $\varphi = 45^\circ$ and $Ra = 10^3$, due to weak circulations, the heat transfer rate slowly increases along the side wall. The heat transfer rate decreases in the lower half of the side walls whereas the increasing trend of heat transfer rate is observed in the upper half of the side walls with $Ra = 10^5$ except for $\varphi = 0^\circ$. The increasing trend of $Nu_s$ is further due to highly compressed isotherms near the top portion of the side walls. Local Nusselt number being negative implies that some part of the heat goes into the lower part of the wall. It is observed that $Nu_s$ gradually increases from negative value and $Nu_s$ becomes positive at distance being 0.6–0.7 and thereafter, $Nu_s$ is larger due to highly compressed isotherms. Due to presence of a pair of symmetric secondary circulation cells with clockwise and anti-clockwise rotations for $\varphi = 0^\circ$, the heat transfer rate is non-monotonic in nature in the lower half of the side walls and the increasing trend of heat transfer rate is observed in the upper half of the side walls only. For $Pr = 10$, the local heat transfer rate of side walls is qualitatively similar to $Pr = 0.7$ (Fig. 11(b)). The isotherms are more dense near the lower part for $Pr = 0.7$ and therefore, $Nu_s$ at the lower portion is larger for $Pr = 0.7$ compared to $Pr = 10$ with $\varphi = 0^\circ$ whereas $Nu_s$ is larger at the top portion due to largely dense isotherms.

### 5.4.2. Local Nusselt number: linearly heated left wall with cold right wall

Fig. 12(a) displays the local heat transfer rate for the bottom wall ($Nu_b$) with $Pr = 0.7$ and $Pr = 10$ and $Ra = 10^3 - 10^5$ for various tilt angles ($\varphi$). Similar to the case with linearly heated side

walls, $Nu_b$ is small for $Ra = 10^3$. The heat transfer rate ($Nu_b$) is minimum at the left-edge of the bottom wall due to linearly heated left wall and maximum at the right-edge of the bottom wall due to the cold right wall at $Ra = 10^5$ for all $\varphi$ and $Pr$. For all the cases, the isotherms near the cold right wall are highly compressed due to the discontinuity at the right edge and that also results in high thermal gradient near the right edge of the bottom wall. The local heat transfer rate around $X \geqslant 0.5$ of the bottom wall is higher for $\varphi = 0^\circ$ due to dense isotherms. It is interesting to observe that qualitative trends on the spatial distributions of $Nu_b$ are similar for $Pr = 0.7$ and 10 with all tilt angles.

Fig. 12(b) illustrates the heat transfer rate for the left wall ($Nu_l$) and it is seen that $Nu_l$ is negative indicating that the heat transfer occurs from fluid to the lower portion of the left wall. Also, the magnitude of $Nu_l$ increases slowly from the bottom edge to the top edge of the left wall for $\varphi = 45^\circ$ and $Ra = 10^3$ and similar variation was also observed as seen in Fig. 11b. The local Nusselt number follows non-monotonic trend for $Ra = 10^5$. The non-monotonic trend is exhibited due to the presence of secondary circulations. Further, the secondary circulations push isotherms at the top edge of the left wall which result in large local Nusselt number. For $\varphi = 0^\circ$, the heat transfer at the bottom edge of the left wall is zero and $Nu_l$ increases sharply near the top edge of the left wall as several isotherms are found to be compressed in a very small regime.

Fig. 12(c) illustrates the heat transfer rate ($Nu_r$) at the right wall. Due to the singularities present in the thermal boundary layer at the right corner of the bottom wall, the heat transfer rate at the right wall is maximum at the bottom edge of the right wall. For all tilt angles, heat transfer rate suddenly decreases at a point near the bottom portion of the wall and that becomes almost constant for $Y \geqslant 0.2$ due to presence of thermal boundary layer. The sudden decrease of $Nu_r$ also corresponds to larger thickness of boundary layer.

*5.4.3. Average Nusselt numbers*

The overall effect upon the heat transfer rates for linearly heated side walls is displayed in Fig. 13(a) and (b) where the distributions of the average Nusselt number of the bottom and side walls are plotted vs the logarithmic Rayleigh number. The average Nusselt numbers are obtained using Eqs. (21)–(23) where the integral is evaluated using Simpsons 1/3 rule. The values of the average Nusselt numbers along the side walls are less compared to the bottom wall. This is due to the fact that the heat transferred to the fluid from the bottom wall is more compared to the side wall. The average Nusselt numbers for both bottom and side walls remain constant up to $Ra = 5 \times 10^3$ for $\varphi = 45^\circ$ and $30^\circ$, and $Ra = 10^4$ for $\varphi = 0^\circ$. The dependence of average Nusselt numbers on the Rayleigh number were found to be significant. It is interesting to note that the smoothness in average Nusselt number curve breaks for $\varphi = 0^\circ$ at $Ra = 7 \times 10^4$ at both bottom and side walls as the oppositely rotated secondary cells becomes prominent.

The overall effects of $Ra$ and $Pr$ on the average Nusselt numbers at the bottom and right walls for linearly heated left wall and cold right wall are displayed in Fig. 13(c) and (d). The average Nusselt numbers for bottom and left walls remain constant up to $Ra = 3 \times 10^3$ for $\varphi = 45^\circ$ and $30^\circ$, and $Ra = 5 \times 10^3$ for $\varphi = 0^\circ$. It is observed that the average Nusselt numbers smoothly increase with $Ra$ for all $\varphi$. The inset of Fig. 13(d) shows the variation of average Nusselt number of right wall. The heat transfer rate increases smoothly with Rayleigh number for all $\varphi$ due to absence of multi-

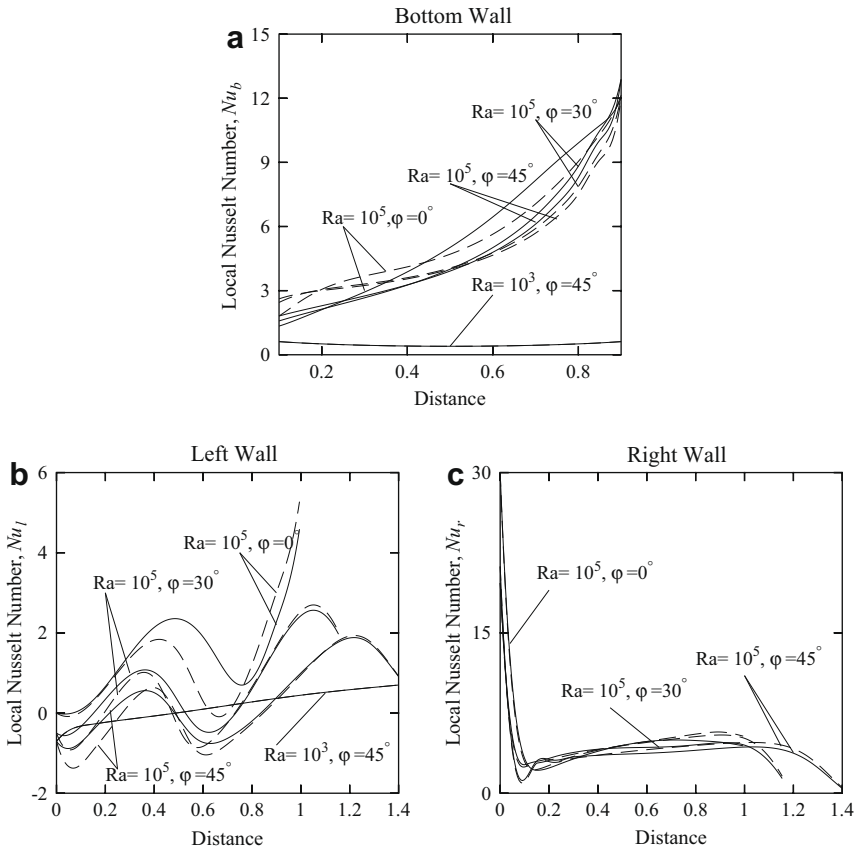


**Fig. 12.** Variation of local Nusselt number with distance along (a) bottom wall (b) left wall and (c) right wall for $Pr = 0.7$ (—) and $Pr = 10$ (- - -) for linearly heated left wall and cold right wall.

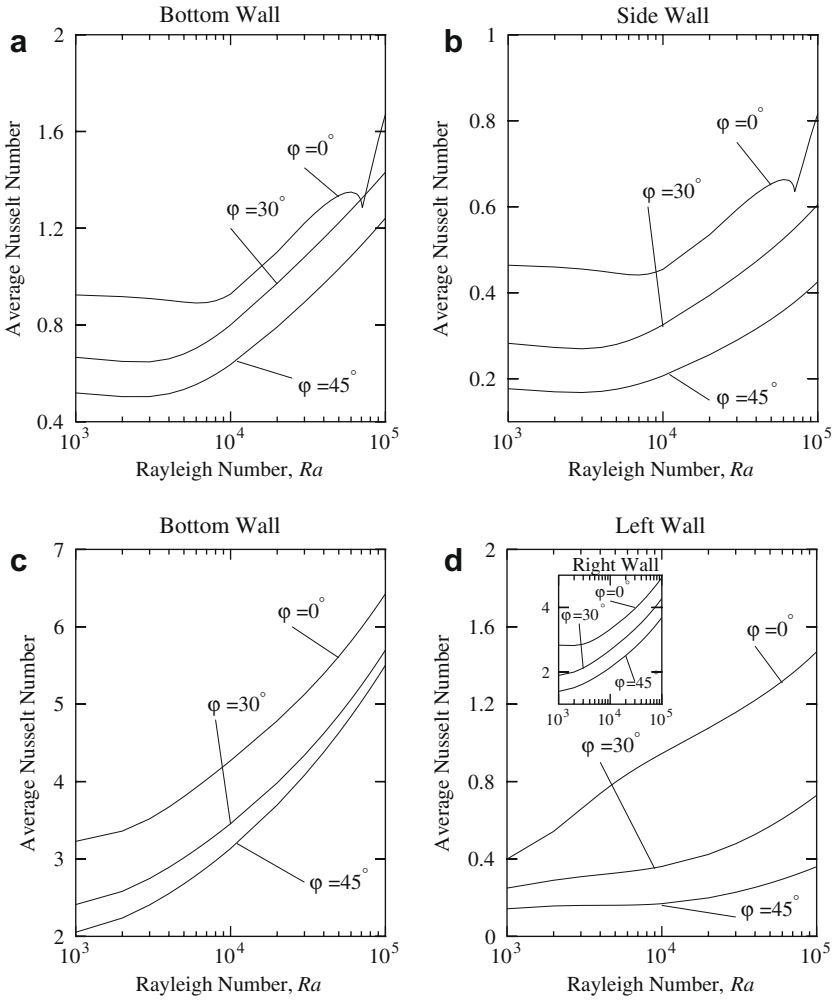


**Fig. 13.** Variation of average Nusselt number with Rayleigh number for linearly heated side walls (a and b) and linearly heated left wall and cold right wall (c and d) for $Pr = 0.7$. The inset of d shows plot of average Nusselt number vs. Rayleigh number for right wall.

ple cells near the right wall. Note that, the average heat transfer rate for the left wall is quite high especially at $Ra \geqslant 10^4$ for $\varphi = 0^\circ$. A power law correlation cannot be obtained for the cases involving linearly heated side walls and linearly heated left wall.

## 6. Conclusion

Role of linearly heated side wall(s) and heat transfer characteristics due to natural convection for various liquids in the trapezoidal enclosure has been studied in details. The penalty finite element method has been used and smooth solutions are obtained in terms of streamlines and isotherms for wide ranges of *Pr* and *Ra*. Numerical simulations were performed for various values of Rayleigh and Prandtl numbers ($10^3 \leqslant Ra \leqslant 10^5$, $0.7 \leqslant Pr \leqslant 1000$) and side wall inclination angles ($\varphi = 45^\circ$, $30^\circ$ and $0^\circ$). For $Pr = 0.7$ and $Ra = 10^3$, stronger convection is observed for $\varphi = 45^\circ$, $30^\circ$ than that for $\varphi = 0^\circ$. At $Ra = 10^5$, the secondary circulations are observed near the bottom corners for $\varphi = 0^\circ$ especially for lower *Pr* fluid with linearly heated side walls. In contrast, for $Ra = 10^5$, stronger secondary circulations are observed near the top portion of the left wall, due to significant low viscous effects for cold right wall and linearly heated left wall. The secondary circulations are stronger for $\varphi = 45^\circ$ and $30^\circ$ and the secondary circulations are even stronger for higher *Pr*. As Prandtl number increases from $Pr = 0.7$ to 1000, the circulations become stronger and the streamlines near the boundary of the cavity are found identical to the shape of the cavity. During conduction dominant regime, variation of tilt angles from $\varphi = 45^\circ$ to $\varphi = 30^\circ$ has less significance.

For the case of linearly heated side walls and linearly heated left wall with cold right wall, the local Nusselt numbers at the side walls and left wall become negative signifying that fluid at lower portion transfers heat to the wall. It is also observed that the heat transfer rate at the top portion of side wall is maximum for $\varphi = 0^\circ$. Reduction in angle from $\varphi = 45^\circ$ to $\varphi = 0^\circ$ enhances the heat transfer rate at bottom wall gradually due to the compression of the isotherms near the central portion of the bottom wall except at corner points. Heat transfer rate for side wall at $Ra = 10^5$ is smaller in the lower half of the side walls, but the increasing trend of heat transfer rate is observed in the upper half of the side walls for linearly heated side walls. For the case of linearly heated left wall and cold right wall, the local Nusselt number at the left wall exhibits non-monotonic behavior due to the presence of secondary circulation attached to linearly heated left wall. Local Nusselt number at the right wall is found to be decreased with distance near the bottom corner whereas that is found to be increased near the top corner point.

Average Nusselt number vs Rayleigh number illustrates that overall heat transfer rate at the bottom wall is higher for the linearly heated left wall and cold right wall. It is also observed that conduction dominant region for both linearly heated side walls is

up to $Ra = 5 \times 10^3$ for $\varphi = 45^\circ$ and $30^\circ$ and $Ra = 10^4$ for $\varphi = 0^\circ$. For linearly heated left wall and cooled right wall, conduction dominant region is up to $Ra = 3 \times 10^3$ for $\varphi = 45^\circ$ and $30^\circ$ and $Ra = 5 \times 10^3$ for $\varphi = 0^\circ$. Role of multiple circulations for $\varphi = 0^\circ$ are found to be important for the non-monotonic variation of average Nusselt numbers versus Rayleigh number and thus power law correlations are not provided for average Nusselt numbers. Ongoing studies also involve to investigate possibilities of multiplicity of steady states and circulations which may appear in future publications.

## Acknowledgment

Authors thank Anonymous reviewers for critical comments and suggestions which improved the quality of the manuscript.

## Appendix A

The name 'isoparametric' derives from the fact that the same parametric function describing the geometry may be used for interpolating spatial variable within an element. Fig. 1a–c show a trapezoidal domain which is mapped to a square domain. The transformation between $(x, y)$ and $(\xi, \eta)$ coordinates can be defined by $X = \sum_{k=1}^{9} \Phi_k(\xi, \eta) x_k$ and $Y = \sum_{k=1}^{9} \Phi_k(\xi, \eta) y_k$ where $(x_k, y_k)$ are the $X, Y$ coordinates of the $k$ nodal points as seen in Fig. 1b and c, and $\Phi_k(\xi, \eta)$ is the basis function. The nine basis functions are:

$$\Phi_1 = (1 - 3\xi + 2\xi^2)(1 - 3\eta + 2\eta^2)$$
$$\Phi_2 = (1 - 3\xi + 2\xi^2)(4\eta - 4\eta^2)$$
$$\Phi_3 = (1 - 3\xi + 2\xi^2)(-\eta + 2\eta^2)$$
$$\Phi_4 = (4\xi - 4\xi^2)(1 - 3\eta + 2\eta^2)$$
$$\Phi_5 = (4\xi - 4\xi^2)(4\eta - 4\eta^2)$$
$$\Phi_6 = (4\xi - 4\xi^2)(-\eta + 2\eta^2)$$
$$\Phi_7 = (-\xi + 2\xi^2)(1 - 3\eta + 2\eta^2)$$
$$\Phi_8 = (-\xi + 2\xi^2)(4\eta - 4\eta^2)$$
$$\Phi_9 = (-\xi + 2\xi^2)(-\eta + 2\eta^2)$$

The above basis functions are used for mapping the trapezoidal domain into square domain and the evaluation of integrals of residuals (Eqs. (11)–(13), (16)).

## References

[1] L. Rabiey, D. Flick, A. Duquenoy, 3D simulations of heat transfer and liquid flow during sterilisation of large particles in a cylindrical vertical can, J. Food Eng. 82 (2007) 409–417.
[2] A.G.A. Ghani, M.M. Farid, X.D. Chen, P. Richards, Numerical simulation of natural convection heating of canned food by computational fluid dynamics, J. Food Eng. 41 (1999) 55–64.
[3] L. Zhang, P.J. Fryer, Models for the electrical heating of solid liquid food mixtures, Chem. Eng. Sci. 48 (1993) 633–642.
[4] A. Jung, P.J. Fryer, Optimising the quality of safe food: Computational modelling of a continuous sterilisation Process, Chem. Eng. Sci. 54 (1999) 717–730.
[5] A.G.A. Ghani, M.M. Farid, S.J. Zarrouk, The effect of can rotation on sterilization of liquid food using computational fluid dynamics, J. Food Eng. 57 (2003) 9–16.
[6] D. Fargue, P. Costeséque, P.H. Jamet, S. Girard-Gaillard, Separation in vertical temperature gradient packed thermodiffusion cells: an unexpected physical explanation to a controversial experimental problem, Chem. Eng. Sci. 59 (2004) 5847–5852.
[7] A. Bejan, Convection Heat Transfer, third ed., Wiley, NJU, Hoboken, 2004.
[8] B. Gebhart, Buoyancy induced fluid motions characteristics of applications technology: The 1978 Freeman Scholar Lecture, ASME Trans. J. Fluids Eng. 101 (1979) 5–28.
[9] C.J. Hoogendoorn, Natural convection in enclosures, Proc. Eighth Int. Heat Transfer Conference, vol. 1, Hemisphere Publishing Corp, San Francisco, 1986. 111–120.
[10] J. Patterson, J. Imberger, Unsteady natural convection in a rectangular cavity, J. Fluid Mech. 100 (1980) 65–86.
[11] V.F. Nicolette, K.T. Yang, J.R. Lloyd, Transient cooling by natural convection in a two-dimensional square enclosure, Int. J. Heat Mass Transfer 28 (1985) 1721–1732.
[12] J.D. Hall, A. Bejan, J.B. Chaddock, Transient natural convection in a rectangular enclosure with one heated side wall, Int. J. Heat Fluid Flow 9 (1989) 396–404.
[13] J.M. Hyun, J.W. Lee, Numerical solutions of transient natural convection in a square cavity with different sidewall temperature, Int. J. Heat Fluid Flow 10 (1989) 146–151.
[14] T. Fusegi, J.M. Hyun, K. Kuwahara, Natural convection in a differentially heated square cavity with internal heat generation, Num. Heat Transfer A – Appl. 21 (1992) 215–229.
[15] J.L. Lage, A. Bejan, The Ra–Pr domain of laminar natural convection in an enclosure heated from the side, Num. Heat Transfer A – Appl. 19 (1991) 21–41.
[16] J.L. Lage, A. Bejan, The resonance of natural convection in an enclosure heated periodically from the side, Int. J. Heat Mass Transfer 36 (1993) 2027–2038.
[17] C.M. Xia, J.Y. Murthy, Buoyancy-driven flow transitions in deep cavities heated from below, ASME Trans. J. Heat Transfer 124 (2002) 650–659.
[18] L. Iyican, Y. Bayazitoglu, An analytical study of natural convective heat transfer within trapezoidal enclosure, ASME Trans. J. Heat Transfer 102 (1980) 640–647.
[19] Y.E. Karyakin, Transient natural convection in prismatic enclosures of arbitrary cross-section, Int. J. Heat Mass Transfer 32 (1989) 1095–1103.
[20] M. Perić, Natural convection in trapezoidal cavities, Num. Heat Transfer A – Appl. 24 (1993) 213–219.
[21] R.A. Kuyper, C.J. Hoogendoorn, Laminar natural convection flow in trapezoidal enclosures, Num. Heat Transfer A – Appl. 28 (1995) 55–67.
[22] H. Sadat, P. Salagnac, Further results for laminar natural-convection in a 2-dimensional trapezoidal enclosure, Num. Heat Transfer A – Appl. 27 (1995) 451–459.
[23] Z.F. Dong, M.A. Ebadian, Investigation of double-diffusive convection in a trapezoidal enclosure, J. Heat Transfer – Trans. ASME 116 (1994) 492–495.
[24] H.D. Nguyen, S. Paik, R.W. Douglass, Double-diffusive convection in a porous trapezoidal enclosure with oblique principal axes, J. Thermophys. Heat Transfer 11 (1997) 309–312.
[25] J.T. Van der Eyden, T.H. Van der Meer, K. Hanjalic, E. Biezen, J. Bruining, Double-diffusive natural convection in trapezoidal enclosures, Int. J. Heat Mass Transfer 41 (1998) 1885–1898.
[26] E. Papanicolaou, V. Belessiotis, Double-diffusive natural convection in an asymmetric trapezoidal enclosure: unsteady behavior in the laminar and the turbulent-flow regime, Int. J. Heat Mass Transfer 48 (2005) 191–209.
[27] E. Papanicolaou, V. Belessiotis, Patterns of double-diffusive natural convection with opposing buoyancy forces: comparative study in asymmetric trapezoidal and equivalent rectangular enclosures, J. Heat Transfer – Trans. ASME 130 (2008) Article No.: 092501.
[28] F. Moukalled, S. Acharya, Buoyancy-induced heat transfer in partially divided trapezoidal cavities, Num. Heat Transfer A – Appl. 32 (1997) 787–810.
[29] F. Moukalled, S. Acharya, Natural convection in trapezoidal cavities with baffles mounted on the upper inclined surfaces, Num. Heat Transfer A – Appl. 37 (2000) 545–565.
[30] F. Moukalled, S. Acharya, Natural convection in a trapezoidal enclosure with offset baffles, J. Thermophys. Heat Transfer 15 (2001) 212–218.
[31] F. Moukalled, M. Darwish, Natural convection in a partitioned trapezoidal cavity heated from the side, Num. Heat Transfer A – Appl. 43 (2003) 543–563.
[32] F. Moukalled, M. Darwish, Natural convection in a trapezoidal enclosure heated from the side with a baffle mounted on its upper inclined surface, Heat Transfer Eng. 25 (2004) 80–93.
[33] F. Moukalled, M. Darwish, Buoyancy-induced heat transfer in a trapezoidal enclosure with offset baffles, Num. Heat Transfer A – Appl. 52 (2007) 337–355.
[34] Y. Varol, H.F. Oztop, I. Pop, Numerical analysis of natural convection in an inclined trapezoidal enclosure filled with a porous medium, Int. J. Thermal Sci. 47 (2008) 1316–1331.
[35] J.N. Reddy, An Introduction to the Finite Element Method, McGraw-Hill, New York, 1993.
[36] S. Roy, T. Basak, Finite element analysis of natural convection flows in a square cavity with non-uniformly heated wall(s), Int. J. Eng. Sci. 43 (2005) 668–680.
[37] T. Basak, S. Roy, A.R. Balakrishnan, Effects of thermal boundary conditions on natural convection flows within a square cavity, Int. J. Heat Mass Transfer 49 (2006) 4525–4535.
[38] J.T. Oden, J.N. Reddy, An Introduction to the Mathematical Theory of Finite Elements, John Wiley & Sons, New York, 1976.
[39] O.C. Zienkiewicz, R.L. Taylor, J.M. Too, Reduced integration technique in general analysis of plates and shells, Int. J. Num. Methods Eng. 3 (1971) 275–290.
[40] G.K. Batchelor, An Introduction to Fluid Dynamics, Cambridge University Press, 1967.
[41] M.M. Ganzarolli, L.F. Milanez, Natural convection in rectangular enclosures heated from below and symmetrically cooled from the sides, Int. J. Heat Mass Transfer 38 (1995) 1063–1073.
[42] M. Hortmann, M. Peric, G. Scheuerer, Finite volume multigrid prediction of laminar natural convection: bench-mark solutions, Int. J. Num. Methods Fluids 11 (1990) 189–207.